Beam-Steering SIW Leaky-Wave Subarray With Flat-Topped Footprint for 5G Applications

Fatemeh M. Monavar, *Student Member, IEEE*, Souren Shamsinejad, *Student Member, IEEE*, Rashid Mirzavand, *Member, IEEE*, Jordan Melzer, and Pedram Mousavi, *Senior Member, IEEE*

Abstract—A novel double-layered vertically stacked substrate integrated waveguide leaky-wave antenna (SIW LWA) is presented. An array of vias on the narrow wall produces leakage through excitation of TE10 fast-wave mode of the waveguide. Attenuation and phase constants of the leaky mode are controlled independently to obtain desired pattern in the elevation. In the azimuth, top and bottom layers radiate independently, producing symmetrically located beams on both sides of broadside. A new near-field analysis of single LWA is performed to determine wavenumbers and as a way to anticipate radiation characteristics of the dual layer antenna. In addition to frequency beam steering in the elevation plane, this novel topology also offers flexibility for multispot illumination of the azimuth plane with flat-topped beams at every φ-cut through excitation of each layer separately or both antennas simultaneously. It is shown that the proposed antenna solution is a qualified candidate for 5G base station antenna (BSA) applications due to its capability of interference mitigation and latency reduction. Moreover, from the point of view of highly reliable connectivity, users can enjoy seamless mobility through the provided spatial diversity. A 15-GHz prototype has been fabricated and tested. Measured results are in good agreement with those of simulations.

Index Terms—5G, array antenna, base station antenna (BSA), frequency scanning antenna, leaky-wave antenna (LWA), phase center, subarray, substrate integrated waveguide (SIW).

I. INTRODUCTION

WITH the emergence of 5G network and its diverse range of applications from medical and household appliances, to mobile communications and safety, introducing a new class of advanced antenna solutions to fulfill the corresponding massive traffic volume and substantial data rate demands seems necessary. Although intensive research is ongoing in outlining 5G requirements from the system perspective, unfortunately, the actual development of antennas and RF compo-

nents for realization of this vision is lagging behind [1]–[3]. It is mainly attributed to the fundamental differences in propagation characteristics, and fabrication constraints exist for such a wide range of high frequencies (namely, 10–100 GHz) [1]. Regarding base station antennas (BSAs), limited study items can be found in the literature [4]–[6] and most of them lack a certain degree of clarification of goals and justification of choice of parameters from the point of view of the network in which the device would be deployed in.

Such practice has been avoided in this paper; hence, our choice of parameters and configuration is done so as to accomplish the best compromise between electromagnetic performance, possible realization in current technology, and also success in terms of network expectations.

In this paper, we propose a novel *15-GHz double vertically stacked substrate integrated waveguide leaky-wave antenna (SIW LWA) subarray*, as shown in Fig. 1(c), and investigate for the first time, the implementation of such a subarray structure as a low-complexity approach to build a cylindrical array suitable for future 5G BSA. Our choice of 15-GHz band is inspired by Ericsson's recent 5G campaign revealing to achieve over 4.5-Gb/s data rate in this spectrum [7]. The proposed antenna provides many unique features as follows.

The SIW structure is appealing due to its simple and cost-effective fabrication process [8]–[11]. Furthermore, its low loss values help to compensate the notoriously high propagation loss at high frequencies [2], [3], [12].

The choice of LWA is in favor of size reduction and simplification as the beam scanning is performed by variation of frequency [13]–[19], thus eliminating the need for complex phase shifters required in counterpart structures, such as phased arrays. Furthermore, it will reduce the complexity of downtilt mechanisms, hence saving the network in terms of latency [1]. The elimination of phase shifters makes the antenna passive, and therefore, low cost mass production becomes a possibility.

Another notable feature of our design is that the two 1-D SIW LWAs of Fig. 1(a) and (b) have separate dynamically controllable illumination spots that when combined in the subarray of Fig. 1(c) will make the exploitation of spatial domain possible. This spatial reuse increases spectrum efficiency and will result in traffic capacity enhancement [1].

In addition to this network-related benefit, the main motive for employing more than one antenna in the subarray configuration of Fig. 1(c) is to equip our structure with azimuth beamforming, a feature that has been neglected in favor of
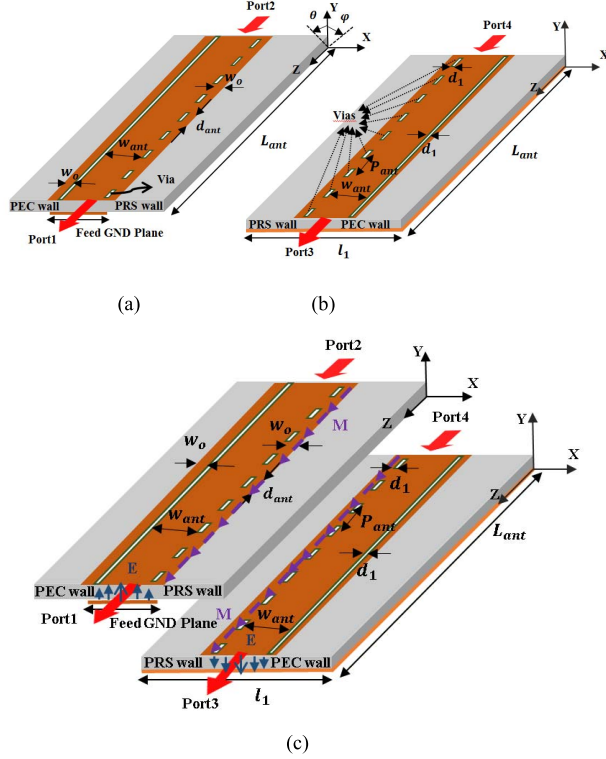
Fig. 1. (a) Top antenna. (b) Bottom antenna. (c) Proposed dual layer subarray. Radiation occurs from the codirected longitudinal magnetic currents M, following Maxwell's equation $M = \hat{n} \times E$ on the two opposite PRS walls. The PRS walls are created by arrays of rectangular vias on $x > 0$ and $x < 0$ on top and bottom SIW LWAs, respectively. Dimensions are as $P_{ant} = 4.5$ mm, $w_{ant} = 7.3$ mm, $w_o = 1.5$ mm, $L_{ant} = 150$ mm, and $l_1 = 28.9$ mm. Substrate thickness for both antennas is 1.575 mm. Each rectangular via has the dimensions of $d_1 = 0.4$ mm and $d_{ant} = 1$ mm and is located at $w_{ant}/2$ away from the center of the waveguide as identified by the curved arrow in (a) and a set of dotted arrows in (b).

leaky-wave elevation beam scanning, in most literature in the area of LWA [19]–[21]. So achieving flexible control of beams in both principal planes is another advantage of our design. Since analogue beamforming is already provided in the subarray, such design can be employed on an array with digital beamformers to realize high-gain multiple-input-multiple-output (MIMO) solutions for low-interference coordination between multiple sites [1]–[5].

Also to overcome challenges associated with the design of the dual layer structure, a novel theoretical study based on near-field monitoring of wavenumbers has been employed. Good correspondence between theoretical and simulated results verified the power of this approach to predict far-field properties of the dual layer subarray.

Other remarkable features include simple feeding, effective use of space through vertically stacked configuration, and the ability to obtain flat-topped beams at every φ-cut in the azimuth. The latter is due to the moving of antenna phase centers [22], on a cylindrical array. This results in link budget improvement, since flat-topped beams experience lower bit error rate (BER) and keep higher signal-to-noise ratio (SNR) [23]. The performance of such a cylindrical array is shown through one example at the end of the manuscript and serves as a springboard to the design of BSAs for

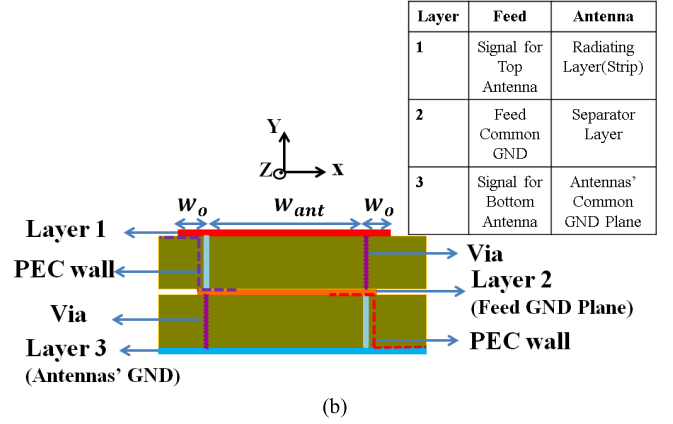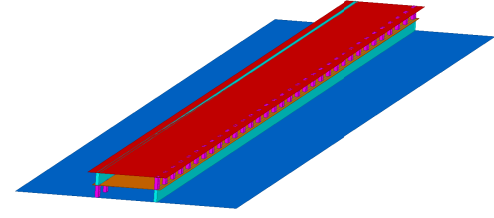| Layer	Feed	Antenna
1	Signal for Top Antenna	Radiating Layer(Strip)
2	Feed Common GND	Separator Layer
3	Signal for Bottom Antenna	Antennas' Common GND Plane

Fig. 2. Proposed dual layer subarray structure. (a) 3-D view. (b) Cross-sectional view. Red and purple dashed lines designate steps in ground plane (layer 3) and radiating strip (layer 1), respectively.

future 5G.

II. DESIGN PROCEDURE

A. Proposed Two-Elements Subarray

The geometry of our proposed double stacked antenna is depicted in Fig. 2(a), where layer 3, shown in blue, and layer 1, shown in red, are the antennas' common ground plane and the common radiating layer, respectively. Fig. 2(b) illustrates the cross section where it is observed how the width of metal layer 1 is extended by w_o from each end. This width w_o is called radiating strip, and is used for tuning purposes to improve antenna radiation efficiency and co to cross polarization ratio. From Fig. 2(b), it is also seen that the two SIWs, each acts as an individual LWA, bonded together through a paper tape, are sharing the mid metal layer; layer 2. This mid layer separates the top and bottom waveguides and it has been cut immediately after the row of vias and the PEC wall on both ends. For fabrication purposes, the width of layer 2 is extended only slightly (1 mm) beyond vias and PEC walls as can be seen in Fig. 2(b).

To create the bottom LWA in our double stacked subarray of Fig. 2(b), the SIW line between metal layers 2 and 3 has been perturbed by introducing a PEC wall at $x > 0$ and an array of sparsely located rectangular vias at $x < 0$. In the same manner, the top SIW LWA has been obtained by integrating a substrate between metal layers 1 and 2; however, the PEC wall and the row of sparse rectangular vias are printed at opposite positions with respect to their counterparts in the bottom LWA. Fig. 2(b) illustrates this situation where for the top SIW LWA, PEC wall and the row of sparse rectangular

vias are shown to be located at $x < 0$ and $x > 0$, respectively. Each of these sparsely located arrays of rectangular-shaped vias is creating a partially reflective surface (PRS) at the lateral edge of the SIW, which will make the radiation possible.

As depicted in Fig. 2(b) and also concluded from description of structures mentioned earlier, the apertures of the top SIW LWA are located between layers 1 and 2 at $x > 0$ whereas for the bottom antenna, apertures are placed between layers 2 and 3 at $x < 0$. It is worth emphasizing that from the perspective of geometry and configuration, top and bottom antennas are distinctly different where the former has a continuous radiating strip but a step ground plane, and the latter has a step radiating strip but a continuous ground plane. The step discontinuity is referred to the substrate thickness that forms a stepped distance between the apertures and their corresponding ground plane (layer 3) or radiating strip at either ends of layer 1.

As stated earlier, both antennas are sharing the mid metal layer; layer 2, which can be conveniently used as a common RF ground plane for the input ports, exciting top and bottom antennas. Hence, electric fields excited in the top and bottom waveguides will have opposite directions as already illustrated in Fig. 1(c). These 180° out of phase input ports will allow for adjusting the main beam direction in the azimuth plane (xy plane) as described in the following.

When port 2 gets excited, main beam is mainly produced by the PRS wall of the top antenna, thus illuminating the first quarter in the azimuth plane, whereas switching the excitation to port 4 will cause the leakage to occur from between the vias on the PRS wall of the bottom antenna, thereby illuminating the second quarter in the azimuth plane. When both antennas are excited simultaneously, these two beams are merged into one perfect flat-topped beam pointed at broadside (y-axis) due to the complete far-field phase cancellation of oppositely directed electric fields from each antenna as will be discussed later in this paper.

The beam in the elevation plane (yz plane) is produced due to the excitation of leaky mode and its pointing angle and beamwidth as will be described in Section II-B, remain constant, and will not be affected by changing excitation at the input ports. So in all three operating modes, i.e., radiation from antenna on top, radiation from the antenna on the bottom, or both simultaneously, this structure yields the same beam in the elevation plane. This condition is ideal, since it means we will observe the same scanning behavior in all three modes as the frequency is changed.

The proposed double stacked structure inspired from the simple single layer antenna introduced in [20]; however, favorable geometrical modifications, as described earlier, have been made to the antenna structure so that to influence radiation pattern in the azimuth plane (azimuth beamforming) without affecting the pattern in the elevation plane and also cross-polarization level.

Our strategy to control over the azimuth plane pattern is proved to be straightforward but extremely effective and it includes applying the steps in the common ground plane (layer 3) and radiating layer (layer 1), stacking up two
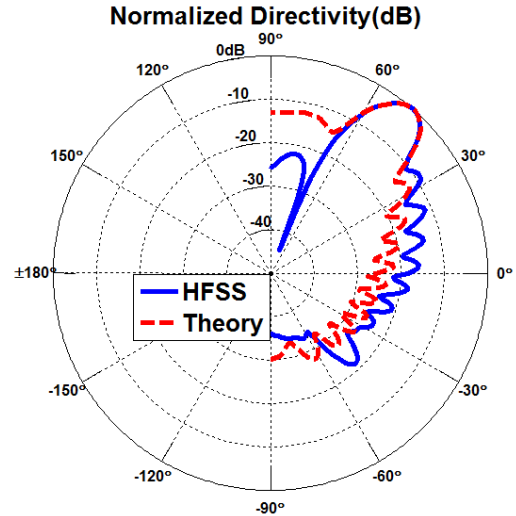

Fig. 3. Radiation pattern of single LWA in the elevation (H-) plane (yz).

antennas, tuning key geometrical parameters such as l_1 and w_o, and also switching the excitation between input ports in order to obtain symmetrically located and flat-topped radiation patterns in the azimuth plane. These aspects will be elaborated in Section IV-A.

B. Single Layer SIW Leaky-Wave Antenna

In this section, full-wave analysis of a single LWA similar to that of Fig. 1(b) is presented except that the PRS is assumed to be on the $x > 0$ wall and the PEC wall on the $x < 0$ lateral edge of the guide. As proved in [8], SIW lines show similar dispersion properties as in standard waveguides for TEn0 modes. So in this antenna, perturbed-TE10 mode is the leaky mode with complex wavenumber $k_z = \beta_z - j\alpha_z$, where β_z is the propagation constant and determines the beam pointing angle in the elevation plane as

$$\beta_z = K_o\sin\theta_{\text{rad}}. \tag{1}$$

Since β_z is related to the waveguide cross section, w_{ant}, and w_{ant}, itself determines the cutoff frequency, for the antenna to work at 15 GHz, and w_{ant} has to be tuned to obtain the main beam at a desired angle [according to (1)] for a certain frequency. Having in mind that, this antenna will be used in a cylindrical configuration mounted on a pole at a base station and will be looking down on the cell site; the pointing angle has been chosen 50° from the antenna broadside (40° from the vertical pole) assuming excitation is placed at port 2. The period P_{ant} between the metallic posts on the lateral wall of the SIW controls the leakage rate and, as a result, will determine the attenuation constant α_z or the imaginary part of the wavenumber. The length of the antenna is selected using (2), such that radiation efficiency is better than 90% for a given attenuation constant at 15 GHz

$$\eta_{\text{rad}} = 1 - e^{-2\alpha_z L_{\text{ant}}}. \tag{2}$$

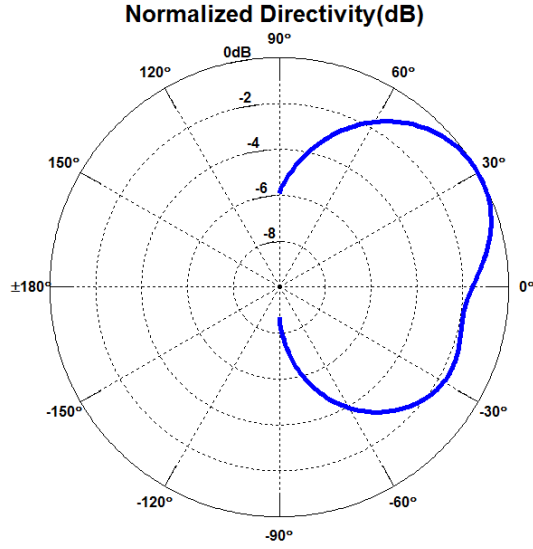In conformity with the most commonly used sector antennas where half power beam width, HPBW $< 15°$, the leaky

Fig. 4. Radiation pattern of single LWA in the azimuth (E-) plane (*xy*).

beamwidth has been chosen $\approx 10°$ using

$$\Delta\theta \approx \frac{\lambda_o}{\cos(\theta_{rad})L_{ant}}. \tag{3}$$

The resulting pattern in the elevation can be seen in Fig. 3.

Essentially, an individual LWA of the form depicted in Fig. 1(a) or (b) can be treated as a linear array along the *z*-axis and an array factor as follows will yield a good approximation of its pattern:

$$AF(\theta) = \sum_{n=1}^{N} I_o e^{-\alpha_z(n-1)P_{ant}} e^{jK_o(n-1)P_{ant}(\sin\theta - \sin\theta_{rad})}. \tag{4}$$

Note that in our problem, the elevation angle θ is separated from the *y*-axis [as shown in Fig. 1(a)]. The beam produced by (4) is also plotted in Fig. 3, indicating a good agreement between the theory and simulation. We, however, notice slight difference in the side lobe levels. The main reasons for such discrepancies (also observed and discussed in [18] and [24]) are summarized in the following.

1) The assumption that array factor could *solely* furnish an accurate representation of the total pattern of the LWA is predicated on the ratio of periodicity over guided wavelength to be much smaller than unity. For $Pant/\lambda_g \approx 0.2$, in our case, the formula in (4), as expected, is only providing a *good approximation* of the pattern especially in the main beam area where the leaky wave is mainly responsible for the radiation.

2) The array factor formula in (4) only considers the leaky-wave wave number whereas in the actual structure, surface-wave is also excited.

This explains the difference in the side lobe levels, since for angles in directions away from the pointing angle, the effect of attenuation constant becomes more pronounced due to the factors, such as excitation of surface-waves, and diffraction effects from finite ground plane. Therefore, all these factors should be considered in order to characterize an accurate representation of the total pattern especially at angles far from the pointing direction.

TABLE I
DIMENSIONS FOR THE SINGLE SIW LWA

Parameter	w_{ant}	P_{ant}	l_1	w_o	d_1	d_{ant}	L_{ant}
Dimension(mm)	7	4	23	1.5	0.1	1	130

Regarding the azimuth pattern of BSA, depending on different antenna alignments and cell shapes, the most frequently reported HPBW values are $30°\sim120°$ [5]. Since the radiating equivalent magnetic current along the *z*-axis produces a fan-shaped beam in the azimuth, as seen in Fig. 4, it provides enough freedom in terms of choosing an optimum value for the horizontal aperture angle appropriate for different propagation environments; urban, suburban, or rural areas. Results of Fig. 4 show that maximum occurs at $\varphi = 30°$ where φ is measured from the *y*-axis. The final optimum values of design parameters are summarized in Table I.

III. NEAR-FIELD ANALYSIS

In this section, a rigorous analysis of electric field in the near field is presented to validate what has already been formulated in Section II-B. It is shown that the near-field data are tremendously powerful in quick prediction of some key features in the far field. Another advantage of near-field analysis is the consideration of the antenna as a whole, which will yield to higher levels of accuracy for determination of attenuation constant α, whereas common dispersion techniques only monitor antenna behavior in one unit cell, which though great for computation of propagation constant β are not perfect solutions for α, since the latter depends on the number of unit cells, edge effects, and mutual couplings not to mention different environment experienced by each unit cell along the antenna length [19].

We see how this refreshing geometrywise monitoring of attenuation and propagation constants helps to extract a ballpark figure on some important features in the far field, such as main beam pointing angles in both principal planes.

Electric field is sampled along lines at regions inside and outside the waveguide to obtain not only the leaky mode wavenumber (along *z*) but also the rate of attenuation for the *E*-field component along other directions (*x* and *y*).

In obtaining the following plots, *E*-field component is considered to be proportional to $E_r \sim A(r)\exp(-j\beta_r - \alpha_r)r$, where *r* could be any *x*, *y*, or *z*. First, we tried to fit this function to the data collected from HFSS. Then, the natural logarithm of the above-mentioned function was taken, and from its real and imaginary parts, attenuation and propagation constants were retrieved as follows:

$$E_y \sim e^{(-j\beta_z - \alpha_z)z}$$
$$\ln E_y \sim -\alpha_z z - j\beta_z z. \tag{5}$$

Attenuation α_z is then obtained from the slope of the line of best fit using the least square technique [18], and β_z is found from period λ_g as in $\beta_z = 2\pi/\lambda_g$. Equation (5) is specified for E_y sampled along *z*. Fig. 5 and plots in Fig. 6(a) illustrate the procedure for a line of sampling (marked with dotted yellow line) located almost $\lambda_r/4$ in front of the apertures at $x = w_{ant} + 3$ mm. This will yield $\alpha_z/K_o \approx 0.032$,
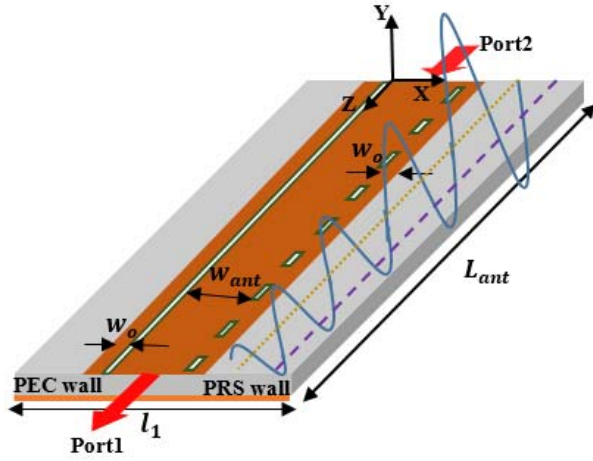
Fig. 5. Illustration of sinusoidal E-field attenuating along the z-axis. Two examples of sampling lines are depicted with dotted yellow and dashed purple lines.

$\lambda_g \approx 25.5$ mm, and $\beta_z/K_o \approx 0.8$, respectively. The same procedure is repeated for E-field values along x and y to find the corresponding wavenumbers in those directions.

After finding α_x, α_y, and α_z, the next step is to study variation of these attenuation constants along different directions as a way to monitor changes in E-field component. Since the amplitude of E-field is a function of the location of the line along which it is sampled, this could be done by moving the line of sampling (as depicted in Fig. 5 with purple dashed line) and collecting E-field samples at various intervals.

Results of such geometry-based monitoring of attenuation constants are given (as α_z as a function of x, α_y as a function of x and z, and finally α_x as a function of z) in Fig. 6(b)–(d), respectively.

The theoretical analysis and geometry are restricted to the case of single layer antenna discussed in Section II-B. However, valuable insights obtained on how manipulation of physical parameters reflects on the far-field behavior, thus helping to overcome challenges associated with multilayer design.

A. Attenuation Along z, α_z

E_y is sampled at periodic distance of P_{ant}, along the guide. The line of sampling is also moved along x-axis (as shown in Fig. 5) and the same data are collected at various x intervals [i.e., $\alpha_z(x)$]. A quick look at the plots in Fig. 6(b) reveals the following key conclusion.

We observe an overall decrease of α_z as x increases. This was expected, since higher attenuation due to the leaky-wave radiation happens at x values closer to the open edge rather than further away in the substrate.

B. Attenuation Along y, α_y

Fig. 6(c) illustrates attenuation experienced by field component along the y-direction. The line along which data are gathered has been moved through different z and x values to obtain $\alpha_y(x, z)$.
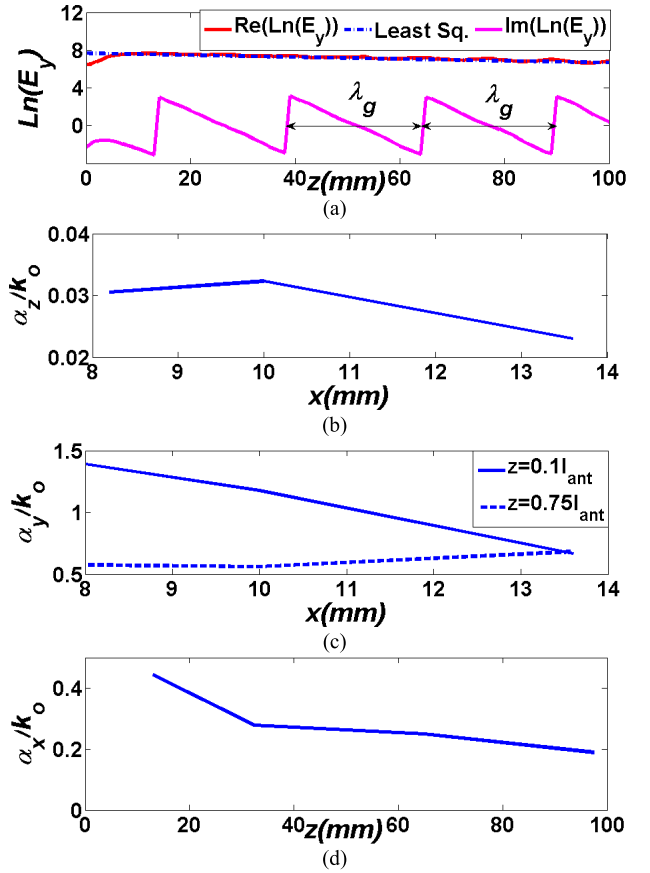

Fig. 6. (a) Sampled near-field data and its least square approximation. (b) Attenuation constant of E-field along the z-direction. (c) Attenuation constant along the y-direction. (d) Attenuation constant along the x-direction.

C. Attenuation Along x, α_x

Fig. 6(d) demonstrates a monotonic decrease of α_x as z is increased. Samples are taken at different z values along the x-direction to yield $\alpha_x(z)$.

D. Impact on the Elevation Plane

We see that at the radiating edge where $x \approx 8$ mm and also along $z = 0.75l_{ant}$ attenuation in all plots is minimum. A reasonable conclusion is that it seems like field components are stronger around this point, so main beam in the elevation plane most possibly occurs in the vicinity of $x \approx 8$ mm and $z = 0.75l_{ant}$. This actually makes sense, since in the elevation plane (yz), radiation is in leaky-wave fashion and leakage happens from between the vias along the z-axis and we expect main beam where at least 70% of power is leaked away so it should be for $z > 0.5l_{ant}$ and in front of the apertures at $x \approx 8$ mm.

To prove this, we attempt to compare near-field data along z, namely, at two values of $z = 0.75l_{ant}$ and $z = 0.1l_{ant}$ to see where in the elevation plane, maximum beam happens. Considering $l_{ant} = 130$ mm, these two points are approximately corresponding to elevation angles of $\theta \approx 50°$ and $\theta \approx -80°$. Since field amplitude will vary along x-direction, we have to choose an appropriate value for x as well. From

Fig. 4, it is seen that maximum far field, due to the pattern having a fan-shaped, occurs at an azimuth plane of $\varphi \approx 30°$ to $\varphi \approx 32°$, and the corresponding x value in the azimuth, considering the dimensions given in Table I, obtains as in $x = 15\sin(30° \sim 32°) \approx 7.5$ mm ~ 8 mm where $(w_{ant}+w_o+0.5(l_1-(w_{ant}+2w_o)))=15$ mm is approximately the distance that the antenna extends along x, from the origin of coordinate system. As stated earlier, electric field amplitude is assumed to be proportional to $E_r \sim A(r)e^{(-j\beta_r-\alpha_r)r}$, where α_r values could be obtained from graphs of Fig. 6. The following observations can be made.

Comparing E-field amplitudes at $z = 0.1l_{ant}$ and $z = 0.75l_{ant}$, we conclude the following.

1) α_z is the same along z(as expected); however, E_y is having smaller values at $z = 0.75l_{ant}$ compared with $z = 0.1l_{ant}$ due to longer z distance.

2) α_y and α_x values at distances further away from the excitation (at $z = 0.75l_{ant}$) are much smaller than at $z = 0.1l_{ant}$. An immediate conclusion is, field components have greater values at $\theta \approx 50°$ compared with $\theta \approx -80°$, which verifies the emergence of main beam around $\theta \approx 50°$ as was anticipated before.

This analysis would help to figure out optimum values for some key parameters, such as l_1 and l_{ant}, to obtain desired radiation properties in the far field. Especially, when two antennas are involved, one could compensate for an attenuating effect on the top layer by small manipulation of geometry on the bottom layer to secure a particular behavior. We also note that whatever the relationship between attenuation constants is, the impact on the E-field amplitude could be stronger due to the added nonlinearity of exponential function.

E. Impact on the Azimuth Plane

From Section III-D and also Fig. 3, we saw that the azimuth pattern is plotted at the maximum of $\theta \approx 50°$, which proved to be approximately along $z = 0.75l_{ant}$. In this section, we compare near-field data along $z = 0.75l_{ant}$ for different x values. The purpose is to prove how copolarized component of E-field maintains almost the same amplitude over a wide range of angles in the azimuth, therefore indicating a fan-shaped beam behavior in the azimuth. Two cases are considered; x values corresponding to $\varphi \approx 35°$ and $\varphi \approx 50°$. Our observations are listed as follows.

1) α_x is the same along x; however, E_y has bigger values at smaller x, i.e., E_y values are greater at $\varphi \approx 35°$ compared with $\varphi \approx 50°$.

2) α_y keeps almost a flat slope as x varies between 9 and 12 mm. Its absolute values shift up a small amount at bigger x values, but the exponential function and, thus, the field amplitude resulting from it do not change effectively along the azimuth plane.

3) α_z compensates for variations made by α_x, since it decreases at higher x values, resulting in greater values for the field components for larger φ values.

Overall, the variation for α_z and α_x tends to almost cancel out the rise and fall in the copolarized component of the field (E_y) over the wide range of azimuth angles. This will
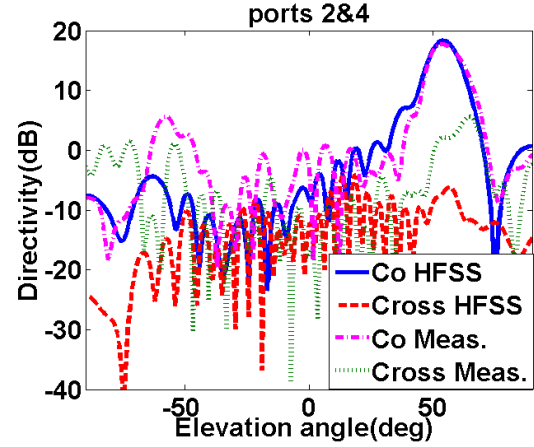

Fig. 7. Comparison of copolarized and cross-polarized components in the elevation plane for the double stacked antenna when both ports are excited.

cause a fan-shaped beam as already seen in the far-field plot of Fig. 4. The range of x values along which α_z and α_x could compensate for variation of E-field depends mostly on w_o and l_1 parameters. This sort of analysis will come in handy when azimuth beamforming is carried out for the dual layer subarray. This aspect is discussed in Section IV.

IV. 2-D MULTIBEAM SUBARRAY PERFORMANCE

A. Simulation

As seen in Section II, an SIW LWA was capable of producing beams pointing at 50° and 30° in the elevation and azimuth planes, respectively. Now if two LWAs of this kind are arranged in a double stacked array, as shown in Fig. 1(c), then it is possible to realize a structure to control beams in both planes through variation of frequency and excitation at input ports. Since the cross section, geometry, and number of vias in both antennas are the same, once excited at input ports, they produce the same propagation constant (β_z) along z, so the main beam pointing angle in the elevation plane, which is a function of β_z will remain the same. It is also worth to mention that due to having the same length, both antennas will experience the same leakage constant, which will yield the same beamwidth in the elevation plane. Based on this, in the elevation plane, we expect quite the same performance from both antennas of the subarray. Both copolarized and cross-polarized patterns are shown in Fig. 7. Frequency scanning of the leaky-wave beam is also depicted in Fig. 8. Details of physical dimensions are listed in the caption of Fig. 1.

Although the beam scanning with frequency is a very attractive feature, since it guarantees that users are receiving maximum power as they move within a coverage cell, but we need to make sure that the beam scanning is not too sensitive to the frequency so the beam does not get deteriorated by small variation of frequency that occurs within the baseband communication channels. Considering the most popular modulation schemes (see [12], [25]) we can safely assume the minimum channel bandwidth to be 50 MHz for which our proposed design shows about 0.5° beam squint that can be easily ignored. From Fig. 8, it can be seen that the main beam angle scans about 10° within 1 GHz. Variation of gain over
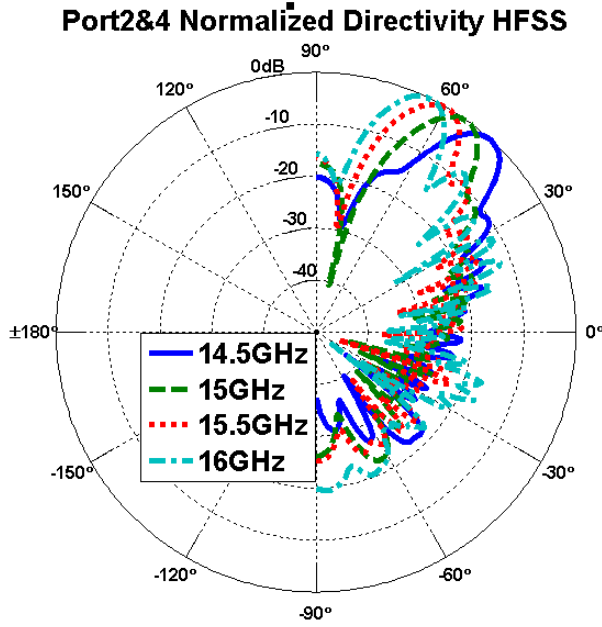
Fig. 8. Simulated frequency scanning behavior in the elevation plane of double stacked antenna when both ports are excited.
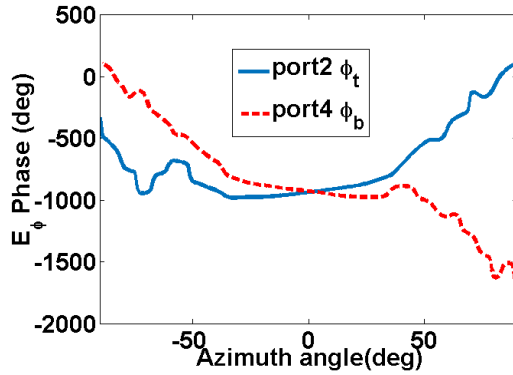

Fig. 9. Continuous far-field phases of top and bottom antennas in the subarray.

this frequency range is about 0.7 dB as it falls from 17.65 dB at 14.5 GHz to 16.93 dB at 16 GHz. The side lobe level also remains below −10 dB for *almost* all angles over the scanning range except for a few angles at 15.5 and 16 GHz, where it reaches the value of −8.24 dB at the highest.

One important parameter here, as pointed out in Section III-E, is l_1 or the substrate width along the x-axis. This will determine the symmetry of (separate) azimuth beams (from each antenna) with respect to the broadside.

The more symmetrically located the main beams are with respect to $\varphi = 0°$, the easier it is to achieve flat-topped main beam at broadside once both antennas are radiating simultaneously. So l_1 has been changed and phase of electric field at $\varphi = 0°$ azimuth in the far field for top and bottom antennas has been recorded separately as φ_t and φ_b. The optimum value for l_1 is obtained when the far-field phases φ_t and φ_b completely cancel each other out at $\varphi = 0°$, as shown in Fig. 9. It would mean that once two antennas are excited simultaneously, the main beam in the azimuth plane appears at
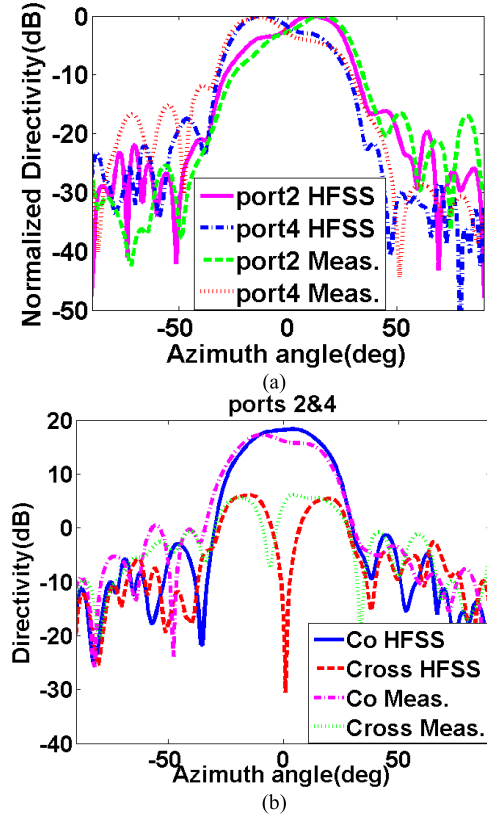

Fig. 10. Azimuth plane patterns. (a) Top and bottom antennas are radiating independently. (b) Copolarized and cross-polarized components when both antennas are excited simultaneously.
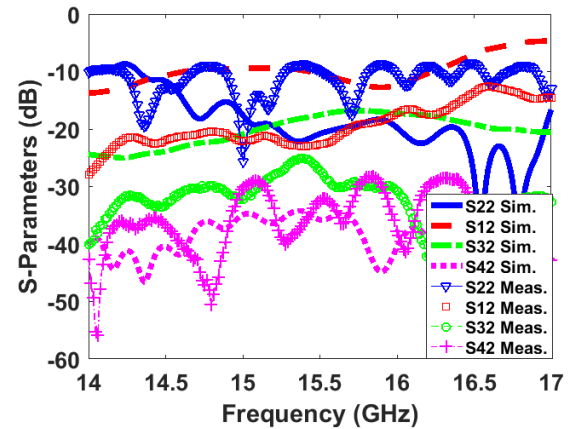
Fig. 11. Simulated and measured S-parameters.

broadside. Graphical representation of such behavior is given by Fig. 10(a) and (b).

Simulated S-parameters are also shown in Fig. 11, where $|S22| \leq -10$ dB over the entire frequency range shows wideband matching performance. It is also seen that the value of $|S12|$ remains almost below −10 dB for the *desired scanning frequency range* (up to 16 GHz), which is an indication of good radiation efficiency, since it would mean that the input power has been considerably reduced due to the leakage, before arriving at the output port. For the higher frequency points in the band, however, $|S12|$ increases due to the stronger and more dominant excitation of the surface-wave and the

Fig. 12. Photograph of the fabricated SIW subarray module. (a) Top layer of board 1. (b) Bottom layer of board 1. (c) Top layer of board 2. (d) Bottom layer of board 2. Board 1 is making the top antenna and board 2 is making the bottom antenna.
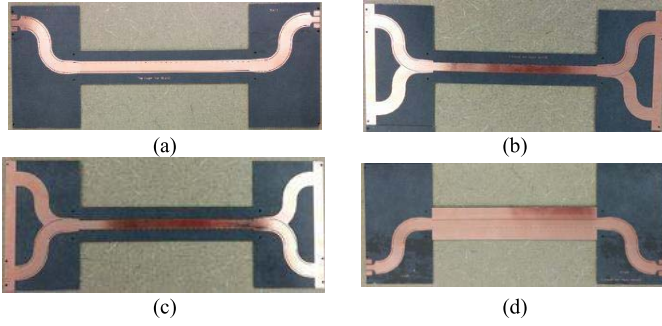

Fig. 13. Gain and radiation efficiency. Solid lines show simulated and dashed-dotted lines represent measured results.

reduction in the radiation leakage as a result of approaching the slow-wave region. This will cause the radiation efficiency and, consequently, the gain to reduce at higher frequencies as will be seen later in Fig. 13.

B. Fabrication and Measurement

PCB process has been used to fabricate each antenna on a single layer RT Doruid 5880 of thickness 1.575 mm, as shown in Fig. 12. Then, both layers are bond together using a paper tape with low dielectric permittivity to implement the dual layer configuration of Fig. 1(c). Measured S-parameters are given in Fig. 11. It is observed that $|S22|$ parameter is mostly better than -10 dB for the entire frequency range of 14–17 GHz. Although, at some frequency points inside the band of interest, its values shift up and reach -8.5 dB at the highest, we still observe an acceptable matching performance. A quick look at Fig. 11 also reveals a difference in the level of $|S22|$ between the simulation and measurement. The main reasons for such discrepancy can be attributed to the loss from the SMA connectors, which are not considered in the simulation and also the fabrication errors in PCB implementation, metallization of vias, and attaching the layers together. The isolation coefficients $|S32|$ and $|S42|$ are below -25 dB within 14–17 GHz. Also note that the insertion loss is better than the simulation results. It is probably due to the added loss from dielectric and metallic parts. The choice of the offset, i.e., the distance required between two SMA connectors, can be used to optimize the total length of bends and tapers to achieve better reflection and insertion loss factors.

The antenna gain and efficiency performance are illustrated in Fig. 13. The simulation plot for radiation efficiency versus frequency is obtained directly from HFSS. In another attempt, we found the residual power by computing the parameter $1-|S22|^2-|S12|^2-|S32|^2-|S42|^2$ which considers the effect of reflected power and the power absorbed in the matched loads. Then, considering the antenna radiation efficiency and the amount of residual power, one can calculate the dissipated power due to the material (conductor and dielectric) loss [16]. Although material loss is higher in fabrication due to the factors, such as roughness of conductors and possibility of nonuniform gaps between the layers, this calculation still provides a good measure of relative loss in practice. Similar to the simulation, residual power can be calculated from
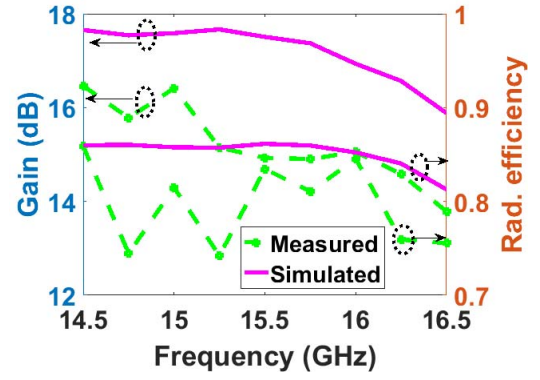
the measured S-parameter data, and then, subtracting the material loss will yield a good approximation of measured radiation efficiency, as illustrated in Fig. 13. Other common methods to determine radiation efficiency of LWAs, apart from calculation of residual power (as in [16] and [26]), include using approximate theoretical formulas [18] or comparison between maximum realized antenna gain and main beam directivity [27]. All these methods have proved to offer trustworthy results for efficiency calculations.

From Fig. 13, it is observed that measured gain and efficiency are above 14 dB and 75%, respectively. The difference between the simulated and measured gains can be attributed to errors in implementation of vias, possibility of nonuniform gap between layers, and overall limited implementation accuracy. Other reasons contributing to this loss of gain in measurement are higher $|S22|$ values due to the loss from SMA connectors and lower $|S12|$ values as a result of more significant conductor and dielectric losses in practice as discussed earlier in this paper. Similar observations on the difference of simulated and measured gain are discussed in the literature. In [16] and [18], they have also investigated the effect of the finite ground plane and proved that the diffractions from the edge of the ground plane are having a more dramatic influence in practice compared with the simulation and could restrict the amount of gain obtained in the measurement.

Measured radiation patterns in the elevation plane compared with the simulation results are already demonstrated in Fig. 7. It can be seen that the antenna is capable of covering the angular region of 10° with its main directivity dropping less than 3 dB. Fig. 7 also indicates that the cross-polarization isolation is better than 14 dB for the entire range of angles.

To study beam steering, radiation pattern in the elevation plane is tested at different frequencies and results are presented in Fig. 14. A quick look at Fig. 14 reveals that the measured patterns present higher side lobe levels compared with the simulated ones in Fig. 8. It can be attributed to metallic parts of the azimuth stage not being perfectly covered during the test and also possible blockage effects due to the power divider and its cables at some angles.

To capture main beam in the azimuth plane, several measurements have been performed to account for the main beam angle pointing at different directions according to the

TABLE II

PERFORMANCE OF THE PROPOSED CYLINDRICAL ARRAY FOR A SCENARIO WHERE USRS ARE SPREAD IN BOTH AZIMUTH AND ELEVATION

$\varphi(deg)$	Subarray switching scheme	Simulation Results of Co-Polarized Gain of One Subarray (dB)						Array switching scheme
		1st floor		2nd floor		3rd floor		
		Send	Receive	Send	Receive	Send	Receive	
95	Ports 2&4	17.4	16.80	17.19	17.26	17.07	16.69	---
90	Ports 2&4	17.65	17	17.58	17.50	17.37	16.89	---
80	Port 2	15.92	15.60	16.1	16.56	16.25	15.49	---
70	Port 2	15.19	14.60	15.05	15.50	15.20	14.40	P12+P24
65	Port 2	12.57	12.65	13.71	13.76	13	12.55	P12+P24

f(GHz): 14.5   14.7   14.9   15.1   15.3   15.5   15.7   15.9   16.1

θ(deg): 48   50   52   54   56   58   60   62   64

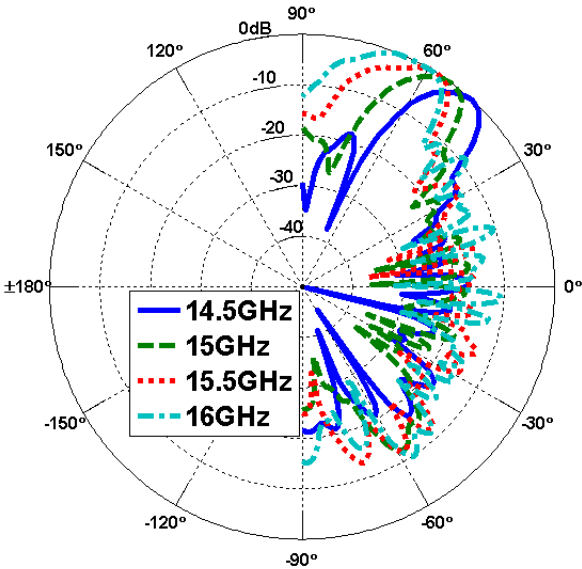Fig. 14.   Measured frequency scanning behavior in the elevation plane of double stacked antenna when both ports are excited.

Fig. 15.   Realization of BSA with an array of eight subarray modules of Fig. 1(c).

corresponding input port. Results are presented in Fig. 10(a) where flat-topped extension of almost 30° is achieved within 3-dB beamwidth of each individual pattern. The value of cross-polarized versus copolarized pattern is also shown in Fig. 10(b) where it reveals isolation better than 12 dB obtained at the main beam angle.

It is worth mentioning that for the case of individual excitation, one port is excited and the other three are terminated with matched loads whereas for the case of simultaneous excitation, a power divider has been used to excite ports 2 and 4 while ports 1 and 3 are terminated with matched loads.

V. APPLICATION TO BASE STATION ANTENNA ARRAY

In this section, we investigate the potential of our proposed design to be used as an element of a BSA array system. Of course, different scenarios have different preferences; regarding the antenna characteristics here, a typical scenario is considered where an array of eight of these antennas could be arranged in a cylinder configuration, as illustrated in Fig. 15. The whole cylinder could then be mounted on a pole to provide the best all-around performance. In this scenario, frequency scanning is done in order for the leaky-wave beam to steer in the elevation plane and choose between different floors of a building, and the users distributed across each floor are then covered using the flat-topped beam of the azimuth plane. Results are given in Table II where in each floor, send and receive channels are assumed to be 400 MHz apart, which could be easily realized by ordinary multiplexers.

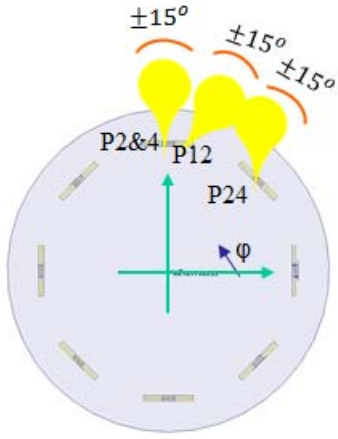Fig. 16. Top view of the cylindrical array and an example of beam interference between neighboring elements according to the array switching scheme given in Table II.

The range in the azimuth indicated with $\pm 15°$ around $80°$.

This $30°$ span of the azimuth angles considered in Table II is for a subarray located at $\varphi = 90°$ in the azimuth, in the eight-element array configuration of Fig. 16.

The gain values given in Table II are, in fact, obtained from one subarray module at different frequencies, and φ-cuts. In order to determine what mode of excitation should be used for the subarray to achieve maximum possible gain at an arbitrary φ-cut, we follow the simple rule as follows. For every φ-cut, the offset between this φ-cut and $\varphi_{\max}$ is calculated where $\varphi_{\max} = 90°$ for simultaneous excitation (ports 2 and 4) and $\varphi_{\max} = 78°$ in the case of individual excitation (port 2); then, the mode of excitation that yields the minimum offset value is selected to illuminate that specific φ-cut. This will yield the subarray switching scheme in the first column of Table II.

Hence, for angles close to broadside ($\varphi = 90°$ and $\varphi = 95°$ as given in Table II), maximum gain is obtained for the case of simultaneous excitation (ports 2 and 4), whereas for the span of angular regions further away from broadside ($\varphi = 80°$ to $\varphi = 65°$), the subarray configuration yields maximum gain if only the top antenna (port 2) is excited.

However, once the subarray is located in the cylindrical array configuration, the contribution from adjacent elements should also be considered and added to the original gain of the subarray. Such situation is illustrated by yellow (interfering) beams in Fig. 16. To get this done, the *subarray switching scheme* in the first column has to be revised to form the *array switching scheme* given in the last column of Table II to include the impact from the neighboring element.

Once beamforming matrices are known, next challenge is to ensure flat-topped coverage in every desired φ-cut. This could be accomplished by beam shaping through the movement of antenna phase centers in the azimuth plane as will be explained in the following.

In Figs. 15 and 16, eight subarray modules are arranged in every $45°$. Considering the 3-dB beamwidth of $30°$, for the observation angles fit in the span of $\pm 15°$ around each subarray's broadside, the possibility of having a flat-topped

beam is seen to be guaranteed, through excitation of both ports in the corresponding subarray [operation on mode 3, see Fig. 10(b)]. In Table II, the first two rows exemplify a situation like this for a module centered at $\varphi = 90°$. Also from the last column, it can be seen that the contribution from neighboring elements over this angular sector is negligible and could be ignored. This is because the $30°$ flat-topped extension of the beam for the neighboring element located at $\varphi = 45°$ will drop more than 3 dB before it can reach the angular regions around broadside of the original element ($\varphi = 90°$, $\varphi = 95°$, and $\varphi = 80°$). So the gain values given for the angles in the first three rows of Table II remain intact and will not be affected by the neighboring elements.

The BSA will change its focus from the span of $30°$ around every $45°$ φ-cut to an angular sector in between two subarrays, if the mode of operation in each subarray changes from simultaneous excitation (mode 3) to one-at-a-time excitation (mode 1 for one subarray and mode 2 for its adjacent neighbor). This will move the phase center in each subarray, from center broadside to a distance in front of its radiating aperture. Such situation is illustrated by purple arrows in Fig. 15 where phase centers from two adjacent contributing elements are moving toward one another, provided that, beam widths and element spacing are well adjusted beforehand, over the angular sector where they almost coincide, a flat-topped beam emerges, illuminating the area. Such constructive interference phenomenon is described in the last two rows of Table II where *Pij* indicates the beam produced by antenna i when port j is excited. Index i takes values of 1 and 2, respectively, for the subarray antenna located at $\varphi = 90°$ and its neighbor at $\varphi = 45°$.

This example shows that the proposed structure is capable of covering the entire azimuth with flat-topped beams and this beam shaping occurs through *virtual* moving of phase centers without actually bending or changing shape, size, or location of antennas in the array. It also proves that our design is well suited for scenarios where users are separated in the horizontal azimuth plane and also shows benefits for vertically configured scenarios, such as coverage of certain high-rise buildings. This configuration is also efficient in terms of keeping the installation and site costs to minimum, since it prevents additional costs associated with mechanisms necessary for deployment of large antennas and also substantial space required for widely spaced arrays.

VI. COMPARISON WITH OTHER BASE STATION ANTENNAS

In this section, we briefly compare the characteristics of our proposed design against other popular types of BSA (given in Table III), such as lens antennas, leaky and traveling wave arrays, patch arrays, and dipole slot arrays. More detailed features are listed in Table III. In listing these criteria in Table III, several fundamental challenges in BSA design are considered. These challenges were identified by considering requirements that would allow 5G to successfully perform its five exemplary scenarios [28]. Some of the challenges are reflecting the link budget related requirements, such as capacity enhancement

TABLE III
COMPARISON BETWEEN DIFFERENT BSAs

Antenna Type	Flat-Topped OR Shaped Beam	Phase Shifters	Feed Simplicity	Dimension OR	Coverage area	Frequency
			Planar	Number of Elements	Beamforming	Gain
Microstrip Patch Phased Array with Adaptive Beamforming [29]	No	Yes	No	$440\ mm \times 320\ mm$ $41\ \lambda_o \times 30\ \lambda_o$	1 km	28 GHz
			Yes	8 Subarrays each made of 4×2 Patch Antennas Total of 64 Elements	Beam Steering	21 dB
Slot Dipole Phased Array [6]	No	Yes	No	$72\ mm \times 52\ mm$ $5.3\ \lambda_o \times 4\ \lambda_o$ $11\ \lambda_r \times 8\ \lambda_r$	$\pm 60^o$ Sector Elevation	22.25 GHz
			Yes	8 Subarrays each made of 1×8 Slot Dipole Antennas Total of 64 Elements	Elevation Beam Steering	19 dB
Switched-Beam Travelling-Wave Microstrip Patch Array [30]	No	No	Yes	$50\ mm \times 25\ mm$ $4\ \lambda_o \times 2\ \lambda_o$ $12.5\ \lambda_r \times 6.25\ \lambda_r$	90° Sector Elevation 60° Sector Azimuth	24 GHz
			Yes	Inner and Outer Subarray made of 1×8 and 1×11 Patch Antennas Total of 19 Elements	Elevation Beam Steering	10 dB
3D Dielectric Lens Antenna [31]	Shaped Beam $sec^2\theta$	No	No	$106\ mm \times 40 mm$ $\times\ 20\ mm$ $21\ \lambda_o \times 8\ \lambda_o \times 4\ \lambda_o$	40 m - 240 m	60 GHz
			No	1 Lens Antenna	Fixed-Beam	11.4 dB
Aperture-Coupled Microstrip Patch Adaptive Antenna [32]	No	Yes	No	$1250\ mm \times 500\ mm$ $7.5\ \lambda_o \times 3\ \lambda_o$	$\pm 60^o$ Sector Azimuth	1800 MHz
			Yes	---	Azimuth Beamforming	22 dB
Aperture-Coupled Microstrip Patch Adaptive Antenna [32]	No	Yes	No	$800\ mm \times 900\ mm$ $2.42\ \lambda_o \times 2.72\ \lambda_o$	$\pm 60^o$ Sector Azimuth	900 MHz
			Yes	---	Azimuth Beamforming	16.5 dB
Our Proposed Leaky-Wave Cylindrical Array	Flat-Topped Beam	No	Yes	$150\ mm \times 28.9\ mm$ $7.5\ \lambda_o \times 1.4\ \lambda_o$ $11.12\ \lambda_r \times 2.14\ \lambda_r$	360° Azimuth 26° Elevation	15 GHz
			Yes	8 Subarrays each made of 2 LWA Total of 16 Elements	Azimuth Beamforming Elevation Beam Steering	17.59 dB

and latency reduction, whereas some others are to address issues, such as network densification to assess if the BSA is efficient in terms of power consumption and realization costs (e.g., how many access points/antenna elements are required for a specific coverage area, availability of low cost and energy-efficient devices). Each class of the BSAs presented in Table III has employed different strategies to overcome design challenges. In the following, we discuss these strategies and also explain how the solutions employed in our proposed design are most likely capable of tackling these challenges.

Flat-Topped Beam: As mentioned in Section I, higher SNR and lower BER can be achieved by transmission of flat-topped beams. This is very beneficial for 5G, since network will be capable of serving more traffic while still maintaining an acceptable SNR, hence increasing the network capacity. Generating flat-topped beam is one of the paramount aspects of our design and is also important from another aspect, solving network densification problem. As proved in [23], flat-topped beams tend to preserve good SNR over wider communication range. Therefore, our BSA is also appropriate for networks

with larger cell size and is capable of providing service over a larger coverage zone.

Phase Shifters: Phased arrays are effective solutions for all cell geometries and environment and the design could be independent of the layout of the coverage area as in [6] and [29]. However, they are not efficient in terms of phase shifters' realization and cost especially at higher frequencies. Furthermore, use of phase shifters makes it difficult to maintain 5G's strict limits of low intermodulation level. In this regard, lobe-switched antennas (as in [30] and this paper) and also fixed-beam lens antennas (as in [31]) are more appropriate choices. In fact, the former has gained a lot of attention in 5G community due to its ability to cover a large sector without having to resort to current inefficient steering solutions, such as low-speed mechanical or costly electronic scanning. However, in both of these cases (switched-beam arrays and lens antennas), unlike the phased arrays, antenna design must be in accordance with the cell configuration.

Low Cost Reproducibility: In general, lens antennas as in [31] and patch arrays as in [30] have the advantage of

low-cost mass production. However, lenses are 3-D structures whereas in many scenarios, planar configurations, such as our proposed design or antennas in [30] and [32], are more favorable choices. Another factor that could affect reproducibility is the feed simplicity. In this regard, the antenna introduced in this paper and also the one in [30] outperforms those of [31] and [32]. This is due to the complicated feeding mechanism provided by 3-D waveguides in [31] and also Butler matrices in [32].

2-D Beam Forming: Beam forming will provide an opportunity for shaping the pattern which among other things results in an efficient use of transmitter power over the coverage area. In our design, it is easily done through the change of phase centers, only by switching excitations at the input ports. In some other antennas, such as adaptive arrays of [32], more complex beamforming networks based on Butler matrices are employed that can dynamically change the pattern; however, due to their complex signal-processing algorithms, they also alter the radiation pattern to some extent. In [31], geometric optics can be used to calculate a surface profile, which will optimally transform radiation of the waveguide feed into the desired coverage. Shaping the 3-D surface of the lens also conveniently compensates path loss and ground reflection. This will keep multipath fading down and, as a result, reduces the delay spread and, hence, number of equalizers required for the network.

High Gain: In general, having a high-gain directive narrow-beam (as produced by LWA in our design and adaptive arrays of [32]) is advantageous due to several reasons, including higher carrier-to-interference (C/I) ratio and better likelihood for line of sight arrival, which will, in turn, reduce the number of parameters that has to be estimated to obtain channel state information [1], [32]. This will also reduce the delay spread and save the network from the excessive use of equalizers. The high-gain beam also allows for additional coverage and, hence, could combat aesthetic difficulties and installation costs associated with densification of networks [32]. Another solution to extend antenna coverage and solve for network densification problem, as mentioned earlier, is by generating flat-topped beams as done in our proposed design.

VII. Conclusion

In this paper, design and implementation of a novel dual layer vertically stacked SIW LWA for future 5G base stations have been proposed. Near-field analysis is employed as a solution to combat difficulties of dual layer design, by providing accurate approximation of wavenumbers for a single layer structure, which will yield conceptual advantage in terms of anticipating the far-field behavior of the double stacked configuration. Simulation and measurement results verified the proposed concept. This architecture is capable of providing service for variety of different scenarios with distribution of users in vertical and/or horizontal plane. The former is shown to be accomplished by frequency scanning of leaky beam in the elevation, whereas the realization of the latter vision has been made possible by multispot flat-topped illumination of the entire azimuth coverage through an arrangement of these antenna modules on a cylindrical array. Though change of details is inevitable for different scenarios, authors believe that strategies and key concepts presented in this paper remain strongly valid to be pursued in future 5G BSA designs.

References

[1] E. Dahlman, S. Parkvall, D. Astély, and H. Tullberg, "Advanced antenna solutions for 5G wireless access," in *Proc. Asilomar ACSSC*, Nov. 2014, pp. 810–814.

[2] D. Muirhead, M. A. Imran, and K. Arshad, "Insights and approaches for low-complexity 5G small-cell base-station design for indoor dense networks," *IEEE Access*, vol. 3, pp. 1562–1572, Aug. 2015.

[3] W. Roh *et al.*, "Millimeter-wave beamforming as an enabling technology for 5G cellular communications: Theoretical feasibility and prototype results," *IEEE Commun. Mag.*, vol. 52, no. 2, pp. 106–113, Feb. 2014.

[4] K. Linehan and J. Robson, "What base station antenna configuration is best for LTE-advanced?" CommScope, Hickory, NC, USA, White Paper WP-106096.1 (12 /16), Sep. 2012.

[5] C. Beckman and B. Lindmark, "The evolution of base station antennas for mobile communications," in *Proc. ICEAA*, Turin, Italy, Sep. 2007, pp. 85–92.

[6] N. Ojaroudiparchin, M. Shen, and G. F. Pedersen, "8 × 8 planar phased array antenna with high efficiency and insensitivity properties for 5G mobile base stations," in *Proc. 10th Eur. Conf. Antennas Propag. (EuCAP)*, Davos, Switzerland, Apr. 2016, pp. 1–5.

[7] J. Gozalvez, "5G tests and demonstrations [mobile radio]," *IEEE Veh. Technol. Mag.*, vol. 10, no. 2, pp. 16–25, Jun. 2015.

[8] F. Xu and K. Wu, "Guided-wave and leakage characteristics of substrate integrated waveguide," *IEEE Trans. Microw. Theory Techn.*, vol. 53, no. 1, pp. 66–73, Jan. 2005.

[9] D. Deslandes, "Design equations for tapered microstrip-to-substrate integrated waveguide transitions," in *IEEE MTT-S Int. Microw. Symp. Dig.*, Anaheim, CA, USA, May 2010, pp. 704–707.

[10] J. Xu, W. Hong, H. Tang, Z. Kuai, and K. Wu, "Half-mode substrate integrated waveguide (HMSIW) leaky-wave antenna for millimeter-wave applications," *IEEE Antenna Wireless Propag. Lett.*, vol. 7, pp. 85–88, 2008.

[11] F. Xu, K. Wu, and X. Zhang, "Periodic leaky-wave antenna for millimeter wave applications based on substrate integrated waveguide," *IEEE Trans. Antennas Propag.*, vol. 58, no. 2, pp. 340–347, Feb. 2010.

[12] W. Hong, K.-H. Baek, Y. Lee, Y. Kim, and S.-T. Ko, "Study and prototyping of practically large-scale mmWave antenna systems for 5G cellular devices," *IEEE Commun. Mag.*, vol. 52, no. 9, pp. 63–69, Sep. 2014.

[13] C. Caloz, T. Itoh, and A. Rennings, "CRLH metamaterial leaky-wave and resonant antennas," *IEEE Antennas Propag. Mag.*, vol. 50, no. 5, pp. 25–39, Oct. 2008.

[14] L. Liu, C. Caloz, and T. Itoh, "Dominant mode leaky-wave antenna with backfire-to-endfire scanning capability," *Electron. Lett.*, vol. 38, no. 23, pp. 1414–1416, Nov. 2002.

[15] Y. Li, Q. Xue, E. K.-N. Yung, and Y. Long, "The periodic half-width microstrip leaky-wave antenna with a backward to forward scanning capability," *IEEE Trans. Antennas Propag.*, vol. 58, no. 3, pp. 963–966, Mar. 2010.

[16] Y. Dong and T. Itoh, "Composite right/left-handed substrate integrated waveguide and half mode substrate integrated waveguide leaky-wave structures," *IEEE Trans. Antennas Propag.*, vol. 59, no. 3, pp. 767–775, Mar. 2011.

[17] J. L. Gómez-Tornero, F. D. Quesada-Pereira, and A. Álvarez-Melcón, "Analysis and design of periodic leaky-wave antennas for the millimeter waveband in hybrid waveguide-planar technology," *IEEE Trans. Antennas Propag.*, vol. 53, no. 9, pp. 2834–2842, Sep. 2005.

[18] J. Liu, D. R. Jackson, and Y. Long, "Substrate integrated waveguide (SIW) leaky-wave antenna with transverse slots," *IEEE Trans. Antennas Propag.*, vol. 60, no. 1, pp. 20–29, Jan. 2012.

[19] A. Grbic and G. V. Eleftheriades, "Leaky CPW-based slot antenna arrays for millimeter-wave applications," *IEEE Trans. Antennas Propag.*, vol. 50, no. 11, pp. 1494–1504, Nov. 2002.

[20] A. J. Martinez-Ros, "Analysis and synthesis of leaky-wave devices in planar technology," Ph.D. dissertation, Dept. Elect. Eng., Polytech. Univ. Cartagena, Murcia, Spain, 2014.

[21] A. M. Patel and A. Grbic, "A printed leaky-wave antenna based on a sinusoidally-modulated reactance surface," *IEEE Trans. Antennas Propag.*, vol. 59, no. 6, pp. 2087–2096, Jun. 2011.

[22] J. U. I. Syed, "Beam shaping by moving the phase center of array antenna," in *Proc. ICMMT*, Beijing, China, Aug. 1998, pp. 349–352.

[23] F. D. Kashani and S. Golmohammady, "Reliability analysis of the flat-topped multi-beam FSO communication link," in *Proc. IST*, Tehran, Iran, Nov. 2012, pp. 500–505.

[24] C. Caloz and T. Itoh, "Array factor approach of leaky-wave antennas and application to 1-D/2-D composite right/left-handed (CRLH) structures," *IEEE Microw. Wireless Compon. Lett.*, vol. 14, no. 6, pp. 247–276, Jun. 2004.

[25] *Laying the Foundations for Next Generation Mobile Services: Update on Bands Above 6 GHz*, Ofcom, London, U.K., 2015, pp. 1–68.

[26] Y. J. Cheng, W. Hong, and K. Wu, "Millimeter-wave half mode substrate integrated waveguide frequency scanning antenna with quadri-polarization," *IEEE Trans. Antennas Propag.*, vol. 58, no. 6, pp. 1848–1855, Jun. 2010.

[27] S. K. Podilchak, L. Matekovits, A. P. Freundorfer, Y. M. M. Antar, and M. Orefice, "Controlled leaky-wave radiation from a planar configuration of width-modulated microstrip lines," *IEEE Trans. Antennas Propag.*, vol. 61, no. 10, pp. 4957–4972, Oct. 2013.

[28] A. Osseiran *et al.*, "Scenarios for 5G mobile and wireless communications: The vision of the METIS project," *IEEE Commun. Mag.*, vol. 52, no. 5, pp. 26–35, May 2014.

[29] F. Aryanfar *et al.*, "Millimeter-wave base station for mobile broadband communication," in *IEEE MTT-S Int. Microw. Symp. Dig.*, May 2015, pp. 1–3.

[30] P. Hallbjorner, M. Bergstrom, M. Boman, P. Lindberg, E. Ojefors, and A. Rydberg, "Millimetre-wave switched beam antenna using multiple travelling-wave patch arrays," *IEE Proc.-Microw., Antennas Propag.*, vol. 152, no. 6, pp. 551–555, Dec. 2005.

[31] C. A. Fernandese, P. O. Frances, and A. M. Barbosa, "Shaped coverage of elongated cells at millimetrewaves using a dielectric lens antennas," in *Proc. 25th Eur. Microw. Conf.*, vol. 1. Sep. 1995, pp. 66–70.

[32] B. Johannisson, "Adaptive base station antennas for mobile communication systems," in *Proc. IEEE-APS Conf. Antennas Propag. Wireless Commun.*, Nov. 1998, pp. 49–52.

Fatemeh M. Monavar (S'12) received the B.Sc. degree in biomedical engineering (bioelectric) from the Amirkabir University of Technology (Tehran Polytechnic), Tehran, Iran, in 2006, and the M.Sc. degree in electrical engineering (communications-fields and waves) from the Iran University of Science and Technology, Tehran, in 2010. She is currently pursuing the Ph.D. degree in electrical engineering (electromagnetics and microwave) with the University of Alberta, Edmonton, AB, Canada.

Her current research interests include antenna analysis and design.

Ms. Monavar was a recipient of the NSERC Industrial Postgraduate Scholarship and the Queen Elizabeth II Graduate Scholarship-Doctoral level.

Souren Shamsinejad (S'12) received the B.Sc. degree in electrical engineering from the Amirkabir University of Technology (Tehran Polytechnic), Tehran, Iran, in 2004, and the M.Sc. degree in electrical engineering (communications-fields and waves) from the Iran University of Science and Technology, Tehran, in 2007. He is currently pursuing the Ph.D. degree in electrical engineering (electromagnetics and microwave) with the University of Alberta, Edmonton, AB, Canada.

His current research interests include active integrated antennas, intelligent small antennas, RF, and optical MEMS.

Mr. Shamsinejad was a recipient of the NSERC Industrial Postgraduate Scholarship and the Alberta Innovates-Technology Future Graduate Student Scholarship.

Rashid Mirzavand (S'09–M'12) received the B.Sc. degree in electrical engineering from the Isfahan University of Technology, Tehran, Iran, in 2004, and the M.Sc. and Ph.D. degrees in electrical engineering (communications-fields and waves) from the Amirkabir University of Technology (Tehran Polytechnic), Tehran, in 2007 and 2011, respectively.

He is currently a Post-Doctoral Fellow with the University of Alberta, Edmonton, AB, Canada. His current research interests include RF, and MMIC circuit and antenna design.

Dr. Mirzavand was a recipient of the AITF Postdoctoral Scholarship.

Jordan Melzer received the B.A.Sc. degree in engineering science from the University of Toronto, Toronto, ON, Canada, in 2000, and the Ph.D. degree in electrical engineering (communications) from the University of Southern California, Los Angeles, CA, USA, in 2006.

He is currently a Senior Engineer with TELUS Communications, Vancouver, BC, Canada.

Pedram Mousavi (M'00–SM'14) received the B.Sc. degree (Hons.) in telecommunication engineering from the Iran University of Science and Technology, Tehran, Iran, in 1995, and the M.Sc. and Ph.D. degrees in electrical engineering from the University of Manitoba, Winnipeg, MB, Canada, in 1997 and 2001, respectively.

He has over 12 years of entrepreneurial academic experience with start-up companies from the University of Waterloo, Waterloo, ON, Canada, and the University of Alberta, Edmonton, AB, Canada. He founded Intelwaves Technologies, Leduc, AB, based on the research that he initiated during his postdoctoral fellowship at the University of Waterloo. He is currently an Associate Professor with the Department of Mechanical Engineering and the NSERC-AITF Industrial Research Chair in intelligent integrated sensors and antennas with the University of Alberta. His current mission is to foster a strong collaboration between industry and academia and stimulate more industry relevant research in wireless technologies. The research conducted through this industrial chair program will allow information and communications technology innovations to be applied to the areas of intelligent integrated sensors and antennas to improve the productivity of the oil-energy sector and to sustain its growth. He has over 120 refereed journal and conference articles and holds several patents in this field. His current research interests include advanced intelligent antenna, microwave and millimetre-waves circuits and systems, UWB radar systems, and 3-D printing electronics.